

Chapter 2

Quantum Cascade Lasers: High Performance Mid-infrared Sources

A superlattice is an artificial semiconductor material consisting of a large number of periods, with each time at least two layers of different materials presenting different gap energies but similar lattice constants. Kazarinov and Suris [1] predicted in 1971 the possibility for a semiconductor superlattice to amplify light using intersubband transitions. However, the first quantum cascade lasers (QCLs) were reported by Faist et al. [2] only in 1994, after significant improvement of the epitaxial growth and development of molecular beam epitaxy (MBE) and metal-organic chemical vapor deposition (MOCVD). After this first QCL in AlInAs/GaInAs emitting up to 8.5 mW peak power around 4.6 μm , in pulsed mode and at 88 K, this technology rapidly developed. Mid-infrared QCLs now exist in several III-V semiconductors, they can operate both in pulsed and continuous-wave (CW) mode, at room-temperature in single- or multi-mode regime, with high powers up to a few watts [3–5].

QCLs emitting in the terahertz (THz) have also been realized [7], i.e. in the wavelength range from 30 μm to 1 mm, although they do not operate at room-temperature yet, because of the appearance of thermal relaxation mechanisms between upper and lower laser levels through optical phonons preventing from population inversion when increasing the temperature. Some solutions exist to operate THz QCLs at room temperature, such as the application of a strong magnetic field above 16 T, in order to suppress the inter-Landau-level non-radiative scattering [8]. Another technique based on difference frequency generation in a mid-IR QCL to obtain room-temperature monolithic THz devices has been proposed [9] and has led to the best output power performances at these wavelengths.

Figure 2.1 presents the QCL performances reported in the literature, over the mid-infrared and THz ranges from 3 to 250 μm and their operating temperature. The graph shows the existence of a wavelength range from 28 to 50 μm where no QCLs were realized: it corresponds to the Reststrahlen band, where the III–V materials are absorbant due to optical phonon absorption. In the following, we will focus on mid-infrared QCLs, since room-temperature operation is more convenient for experimental work.

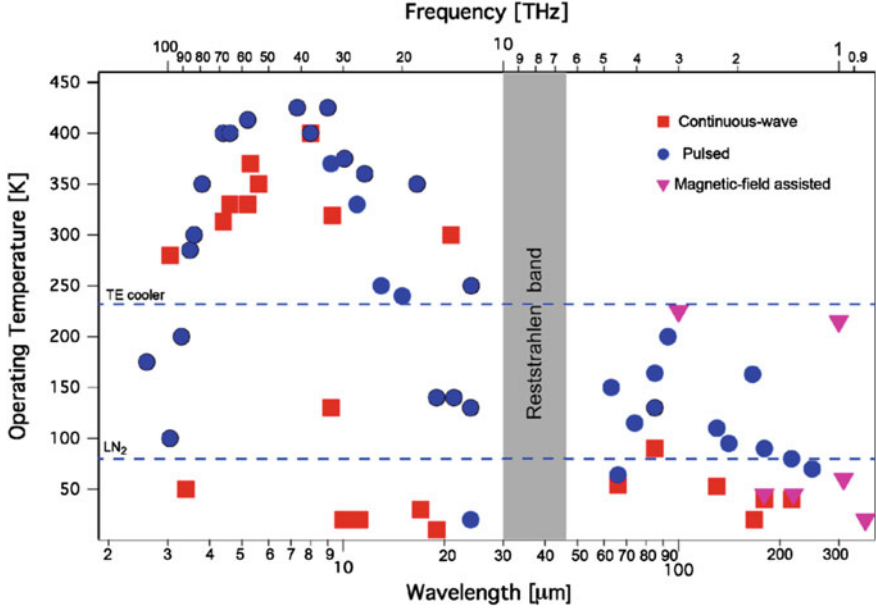


Fig. 2.1 QCL performances reported in the literature, as a function of wavelength and operating temperature (courtesy of [6])

This chapter will present the principle of operation and theory of QCLs. The α -factor, key parameter of semiconductor lasers but not well-known in QCLs, will then be defined, before studying in details a specific QCL structure, from which both Fabry-Perot (FP) and distributed feedback (DFB) devices emitting around $5.6 \mu\text{m}$ were fabricated.

2.1 Principle of Operation

In interband laser diodes, the laser transition occurs between the conduction band and the valence band of the semiconductor material, and the laser frequency ν is determined by the energy gap E_g between these two bands, with the relation $E_g \leq h\nu \leq F_c - F_v$, with F_c and F_v the quasi-Fermi levels associated with the conduction and valence bands, respectively. The laser diode wavelengths are therefore limited below $2 \mu\text{m}$, because the energy gaps of the III–V materials are in this range. On the other hand, QCL operation is based on intersubband transitions within the conduction band of the III–V semiconductor, as shown in Fig. 2.2. Therefore, the emission wavelength is no longer limited by the gap of the material but by the energy spacing between the subbands, which is determined by quantum engineering of the active area. The only limitation in wavelength is the thickness of the quantum well where the laser transition takes place, which rules the spacing between the subbands: if the quantum well is too narrow, the upper subband will be too close to the contin-

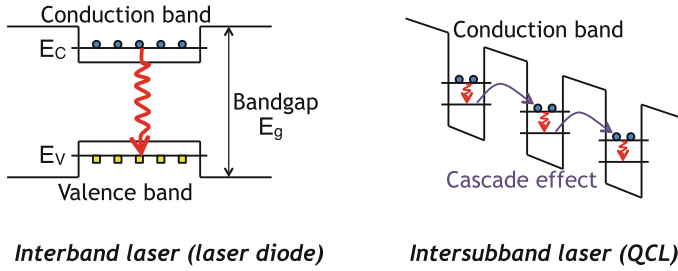


Fig. 2.2 Intersubband transitions and cascade effect

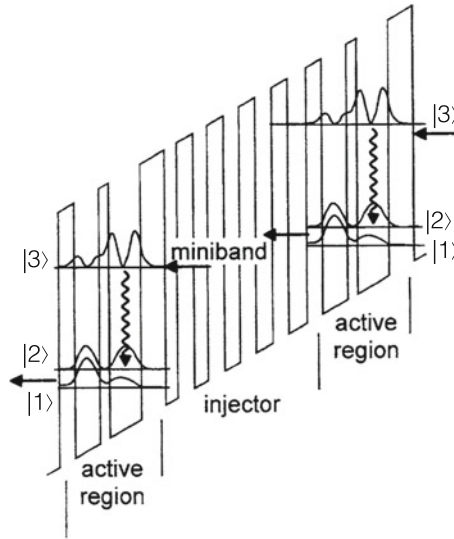


Fig. 2.3 Schematic of a QCL structure, including the wave functions in the active area (courtesy of [11])

uum, the electron will no longer be confined and no photon will be emitted. There are therefore no QCLs emitting below $3 \mu\text{m}$ at room temperature, and the ones emitting between 3 and $4 \mu\text{m}$ are mostly based on newly developed structures containing antimony [10]. On the contrary, if the quantum well is too wide, the subbands will be very close from one another and thermal relaxation will compete with the radiative transitions, hence limiting the operation of THz QCLs to cryogenic temperatures.

A cascading effect is added to the structure in order to improve the efficiency, as shown in Fig. 2.2. Each electron will cascade through several active regions and will each time produce a photon. A QCL is typically constituted of 20 to 40 periods and the electrons transfer from one active region to the other through tunneling effect.

As shown in Fig. 2.3, the actual design of a QCL structure is much more complex than previously described. The laser transition indeed occurs in a multi-quantum well

active region that is a 3-level laser [11]: the photon is emitted during the transition from an upper level $|3\rangle$ to a lower level $|2\rangle$. Then the electron relaxes through an optical phonon in level $|1\rangle$, from which it will tunnel into a injector region, i.e. a succession of narrow quantum wells called minibands that will lead the electron to the upper level $|3\rangle$ of the next active region.

2.2 Theory

2.2.1 Heterostructure

The active region of a QCL is a heterostructure, which allows to confine the electrons along the growth direction. This one-direction confinement leads to discrete energy levels. In the slowly varying envelope approximation, the eigenstates of the heterostructure can be expressed as [12]:

$$\psi(\mathbf{r}) = \sum_m \varphi_m(\mathbf{r}) u_{m,\mathbf{k}=0}(\mathbf{r}) \quad (2.1)$$

where m is one of the band taken into account for the calculation, $u_{m,\mathbf{k}=0}(\mathbf{r})$ is the Bloch function and $\varphi_m(\mathbf{r})$ is a slowly varying envelope. The Bloch functions are assumed to be similar in all the layers of the heterostructure. Therefore, due to the translation invariance in the plane of the layers:

$$\varphi_m(\mathbf{r}) = \frac{1}{\sqrt{A}} e^{i\mathbf{k}_{\parallel}\mathbf{r}_{\parallel}} \chi_m(z) \quad (2.2)$$

with A the area of the laser, $\mathbf{k}_{\parallel}\mathbf{r}_{\parallel} = k_x x + k_y y$ and χ_m an envelope function for the band m .

The conduction band component $\chi_c(z)$ of this equation has to satisfy the Schrödinger-like equation [13]:

$$\left[-\frac{\hbar^2}{2} \frac{d}{dz} \left(\frac{1}{m^*(E, z)} \frac{d}{dz} \right) + E_c(z) \right] \chi_c(z) = E \chi_c(z) \quad (2.3)$$

where $m^*(E) = m^*(E_c) \left[1 + \frac{E-E_c}{E_G} \right]$ is the effective mass, that is a function of the energy to express the band non-parabolicity.

When assuming $\mathbf{k}_{\parallel} = 0$ and a constant effective mass m_{eff} , i.e. parabolic bands, the energies E_k of the band k are given by:

$$E_k = \left(\frac{\hbar^2 \pi^2}{2m_{eff} l^2} \right) k^2 \quad (2.4)$$

with l the quantum well width. The energy of the produced photon $E_{phot} = h\nu$, ν being the frequency, corresponds to the energy difference between two consecutive subbands of the conduction band. For instance, for $k = 2$:

$$E_{phot} = E_2 - E_1 = \frac{3\hbar^2\pi^2}{2m_{eff}l^2} \quad (2.5)$$

2.2.2 Spontaneous Emission and Material Gain Calculation

The electromagnetic wave at frequency ν will interact with the two subbands i and f of the conduction band. The stimulated emission rate $W_{i \rightarrow f}^{st}$ can be expressed as a function of the spontaneous emission rate $W_{i \rightarrow f}^{sp}$ as [14]:

$$\frac{1}{\tau_{if}^{st}} = W_{i \rightarrow f}^{st} = W_{i \rightarrow f}^{sp} \frac{3c^2}{8\pi h\nu^3 n^2} E(\nu) \quad (2.6)$$

where c is the light velocity, $E(\nu)$ the energy density of the wave at frequency ν and n the refractive index.

The energy density can be written as $E(\nu) = L(\nu)I(\nu)$ with $I(\nu)$ the light intensity propagating in the structure and $L(\nu)$ the lineshape function of the energy, corresponding to the width of the energy level due to the electron lifetime. In a QCL, the broadening of the energy level is homogeneous, and $L(\nu)$ has the shape of a lorentzian, as shown in Fig. 2.4b:

$$L(\nu) = \frac{2}{\pi} \frac{\gamma_{if}}{(\nu - \nu_0)^2 + \gamma_{if}^2} \quad (2.7)$$

The optical power can be expressed both as a function of the electron density multiplied by the photon energy and as the product between the material gain and the intensity, following Beer-Lambert's law. Therefore:

$$P_{opt} = (N_i W_{i \rightarrow f}^{st} - N_f W_{f \rightarrow i}^{st}) h\nu = \Delta N W_{i \rightarrow f}^{st} h\nu = g(\nu) I(\nu) \quad (2.8)$$

with N_i and N_f the carrier density of levels i and f , $\Delta N = N_i - N_f$.

This lead to the following expression for the material gain:

$$g(\nu) = W_{i \rightarrow f}^{sp} \frac{3c^2}{8\pi\nu^2 n^2} \Delta N L(\nu) \quad (2.9)$$

Furthermore, the rate of spontaneous emission can be expressed by applying Fermi's golden rule to the electric dipole hamiltonian $H_{DE} = -q\mathbf{E} \cdot \mathbf{r}$ [13]:

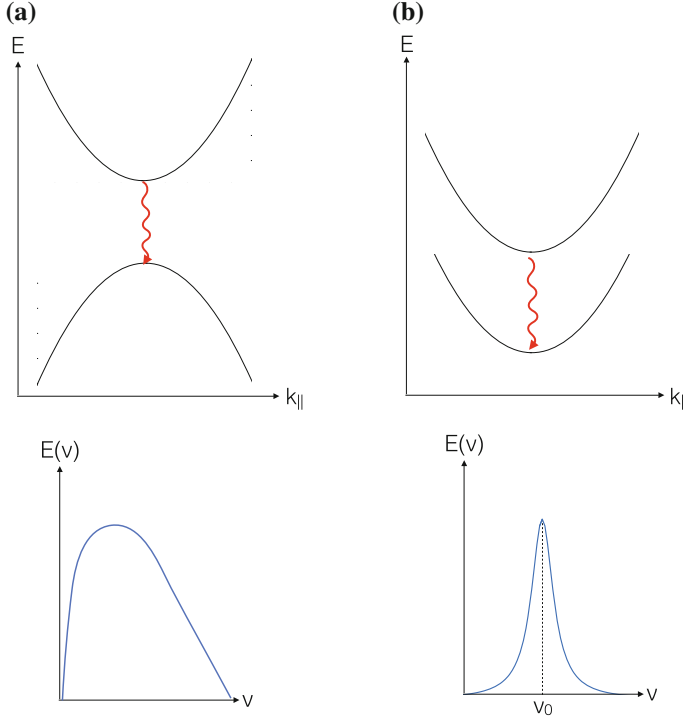


Fig. 2.4 Comparison between interband laser (a) and QCL (b). The upper curves represent the place where the lasing transition takes place, and the lower ones show the energy density $E(\nu)$

$$\frac{1}{\tau_{sp}} = W_{i \rightarrow f}^{sp} = \frac{q^2 n}{3\pi c^3 \epsilon_0 \hbar^4} (h\nu)^3 |z_{if}|^2 \quad (2.10)$$

where q is the elementary electron charge, ϵ_0 the vacuum permittivity and $|z_{if}|$ the dipole matrix element, which is inversely proportional to ν [13, 15]. Therefore, the material gain is directly proportional to $L(\nu)$ and can be written as:

$$g(\nu) = \frac{2\pi^2 q^2}{\epsilon_0 n h c} \nu |z_{if}|^2 \Delta N L(\nu) \quad (2.11)$$

The gain of a QCL has therefore the shape of a Lorentzian, centered around a value ν_0 that depends on the active region materials and on the dimensions of the quantum wells.

2.2.3 QCL Rate Equations

In a QCL, each active region is a 3-level laser. Assuming that all active regions are identical, the rate equations for carriers and photons in active region j can be expressed as [16]:

$$\frac{dN_3^j}{dt} = \eta \frac{I_{in}^j}{q} - \frac{N_3^j}{\tau_{32}} - \frac{N_3^j}{\tau_{31}} - G_0 \Delta N^j S^j \quad (2.12)$$

$$\frac{dN_2^j}{dt} = \frac{N_3^j}{\tau_{32}} - \frac{N_2^j}{\tau_{21}} + G_0 \Delta N^j S^j \quad (2.13)$$

$$\frac{dN_1^j}{dt} = \frac{N_3^j}{\tau_{31}} + \frac{N_2^j}{\tau_{21}} - \frac{I_{out}^j}{q} \quad (2.14)$$

$$\frac{dS^j}{dt} = \left(G_0 \Delta N^j - \frac{1}{\tau_p} \right) S^j + \beta \frac{N_3^j}{\tau_{sp}} \quad (2.15)$$

where N_k^j is the carrier density of level k , $\Delta N^j = N_3^j - N_2^j$. I^j is the bias current entering the active region j . η is the conversion efficiency, τ_{kl} corresponds to the carrier lifetime from level k to level l , τ_{sp} is the spontaneous emission lifetime, τ_p is the photon lifetime inside the laser cavity and β the spontaneous emission factor, which represents the fraction of spontaneous emission coupled into the lasing mode. G_0 corresponds to the net modal gain over one period normalized by the group velocity v_g , expressed in s^{-1} , and can be defined as [16]:

$$G_0 = \frac{\Gamma_{opt} v_g g}{\Delta N^j A} \quad (2.16)$$

with Γ_{opt} the confinement factor, v_g the group velocity, g the gain in cm^{-1} and A the area of the laser cavity. Let us stress that the rate Eqs. 2.12–2.15 correspond to the single-mode scenario. In case of multimode operation, the photon rate equation for each mode can be obtained by adding to the single-mode photon density a term S_m , corresponding to the photon population for the m^{th} longitudinal mode oscillating at the frequency ω_m [17].

In Eqs. 2.12–2.15, the electron will escape from level N_1^j to enter level N_3^{j+1} . Therefore:

$$\frac{I_{out}^j}{q} = \frac{N_1^j}{\tau_{out}} \quad (2.17)$$

$$\frac{I_{in}^j}{q} = \frac{N_1^{j-1}}{\tau_{out}} \quad (2.18)$$

where τ_{out} is the characteristic time for the electron to tunnel into the injector.

This complete QCL model leads to complicated resolution, since $4 \times N_{pd}$ have to be taken into account, with N_{pd} the number of periods. Therefore, the QCL is often considered as a global virtual 3-level system ruled by:

$$\frac{dN_3}{dt} = \eta \frac{I}{q} - \frac{N_3}{\tau_{32}} - \frac{N_3}{\tau_{31}} - G_0 \Delta N S \quad (2.19)$$

$$\frac{dN_2}{dt} = \frac{N_3}{\tau_{32}} - \frac{N_2}{\tau_{21}} + G_0 \Delta N S \quad (2.20)$$

$$\frac{dN_1}{dt} = \frac{N_3}{\tau_{31}} + \frac{N_2}{\tau_{21}} - \frac{N_1}{\tau_{out}} \quad (2.21)$$

$$\frac{dS}{dt} = \left(N_{pd} G_0 \Delta N - \frac{1}{\tau_p} \right) S + \beta \frac{N_3}{\tau_{sp}} \quad (2.22)$$

This simplified model is most of the time sufficient and gives accurate results, as shown in Fig. 2.5. However, for some calculations such as small-signal analysis, it is better to consider the full model, since key parameters such as the time for the electrons to pass through the successive active regions and injectors are not taken into account in the simplified model.

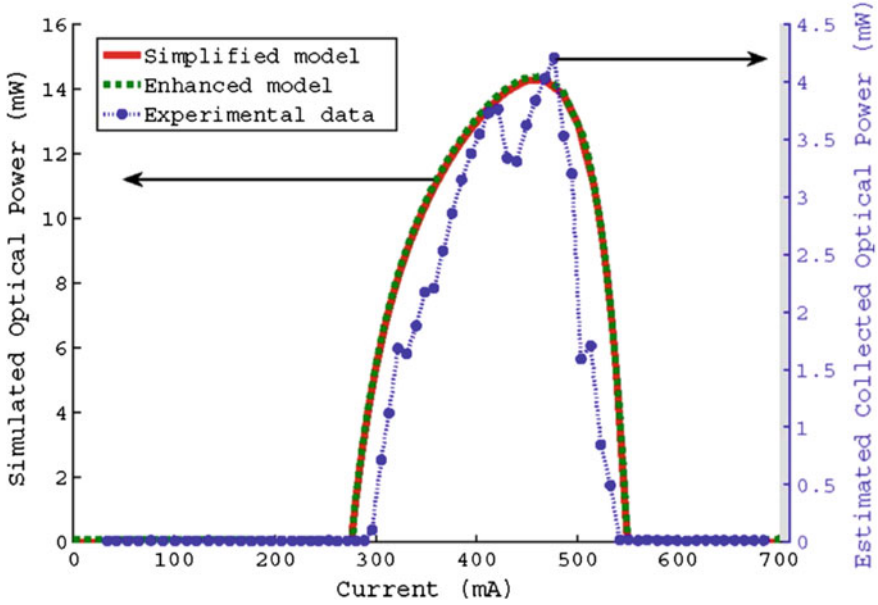


Fig. 2.5 Comparison between complete set of equations and simplified model (courtesy of [16])

2.2.4 QCL Modulation Response

A small-signal analysis of the QCL is realized, by considering small variations around the steady-state values $N_i^j = N_{i,st}^j + \delta N^j$, where $i = 1, 2, 3$ and j the period number, and $S = S_{st} + \delta S$. Under external perturbation $I = I_0 + \delta i$, using the full set of rate equations, the modulation response of a QCL can be written as [18]:

$$H(j\omega) = \frac{\omega_r^2}{\omega_r^2 - \omega^2 + j\omega\Gamma} \quad (2.23)$$

with:

$$\omega_r^2 = \frac{\frac{1}{\tau_p \tau_{st}} \left(1 + \frac{\tau_{21}}{\tau_{31}}\right)}{1 + \frac{\tau_{21}}{\tau_{31}} + \frac{\tau_{21}}{\tau_{32}} + \frac{\tau_{in}}{\tau_3} + \frac{\tau_{21}}{\tau_{st}} \left(2 + \frac{\tau_{in}}{\tau_3}\right)} \quad (2.24)$$

$$\Gamma = \frac{\frac{1}{\tau_{st}} \left(1 + \frac{\tau_{21}}{\tau_{31}}\right) + \frac{1}{\tau_{31}} + \frac{1}{\tau_{32}} + \frac{\tau_{21}}{\tau_p \tau_{st}} \left(2 + \frac{\tau_{in}}{\tau_3}\right)}{1 + \frac{\tau_{21}}{\tau_{31}} + \frac{\tau_{21}}{\tau_{32}} + \frac{\tau_{in}}{\tau_3} + \frac{\tau_{21}}{\tau_{st}} \left(2 + \frac{\tau_{in}}{\tau_3}\right)} \quad (2.25)$$

where $1/\tau_3 = 1/\tau_{31} + 1/\tau_{32}$, τ_{in} is the characteristic time for the electron to tunnel from the injector into the upper level and τ_{st} is the differential lifetime associated with stimulated and spontaneous photon emission [18].

The eigenvalues that drive the damping of perturbations applied to the laser steady-states can be written as:

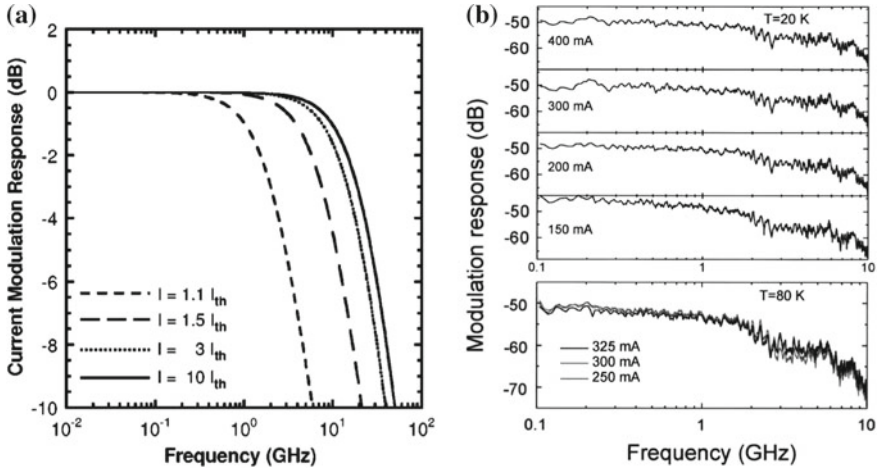


Fig. 2.6 **a** Numerical modulation response (courtesy of [18]). **b** Experimental modulation response (courtesy of [19])

$$f_{\pm} = -\Gamma \pm \sqrt{\Gamma^2 - f_r^2} \quad (2.26)$$

where $f_r = \omega_r/2\pi$ is a characteristic frequency, typically called relaxation oscillation frequency in interband lasers, and Γ is the damping rate, which is much higher than the characteristic frequency in a QCL. The eigenvalues are therefore real since the term under the square root remains always positive. Hence, no relaxation oscillations appear on the modulation response of a QCL, both numerically and experimentally [19], as shown in Fig. 2.6.

2.3 Linewidth Enhancement Factor

2.3.1 Definition

Also called linewidth broadening factor or α -factor, the linewidth enhancement factor (LEF) is an important parameter for semiconductor lasers. It quantifies the coupling between the real and imaginary parts of the nonlinear susceptibility, i.e. between the differential gain and the refractive index, or equivalently the coupling between the amplitude and the phase of the electric field in the laser cavity.

$$\alpha = -\frac{d[\Re(\chi(N))]/dN}{d[\Im(\chi(N))]/dN} = \frac{-4\pi}{\lambda} \frac{dn/dN}{dg/dN} \Leftrightarrow \frac{d\phi/dt}{dI/dt} = \frac{\alpha}{2I} \quad (2.27)$$

The α -factor quantifies the minimum linewidth that can be achieved for a semiconductor laser: compared to the intrinsic linewidth limit defined by Schawlow and Townes [20], the limit linewidth for a semiconductor laser is broadened by a factor $(1 + \alpha^2)$, hence the name given to this parameter. It was first introduced simultaneously in May 1967 by Lax [21] and Haug and Haken [22]. Using either a classical approach based on density matrix calculations or a semi-classical approach based on quantum mechanics, they both introduced a term $(1 + \alpha^2)$ in the theoretical expression of the noise-induced phase fluctuations, that also appears in the linewidth expression. However, the former did not further exploit the obtained linewidth expression, whereas the latter assumed that the LEF was very small compared to 1 and neglected it. In 1982, Henry [23] reintroduced the α -factor and compared his theoretical linewidth expression with several experimental linewidth measurements, resulting in LEF values around 2 to 5 for interband semiconductor lasers.

The α -factor also impacts many important aspects of the semiconductor lasers, such as brightness, modulation properties or filamentation in broad-area semiconductor lasers [24]. Furthermore the LEF significantly influences the nonlinear dynamics of a semiconductor laser subject to optical injection or optical feedback, and nonlinear dynamics can only be observed in lasers for which $\alpha > 0$ [25].

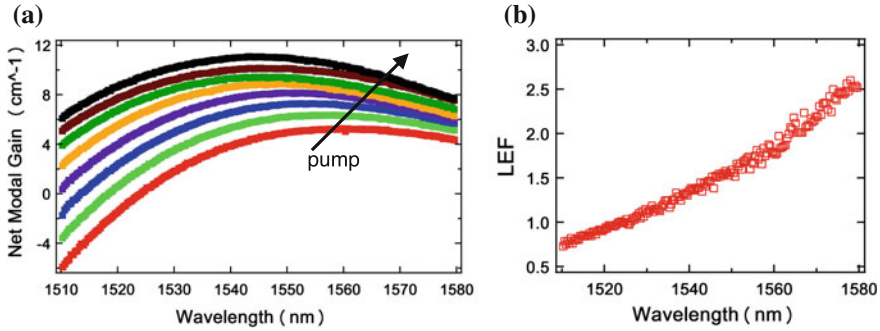


Fig. 2.7 Illustration of the Hakki-Paoli method for a quantum dot laser. **a** Gain shift as a function of the sub-threshold bias current. **b** Deduced α -factor. (Courtesy of [28])

2.3.2 Measurements Methods

As seen in the previous paragraph, the α -factor can be retrieved directly from linewidth measurements. However, this method can be complex to implement, and other measurements techniques have been proposed.

The most common method to measure the linewidth broadening factor was developed by Hakki and Paoli [26] and Henning [27]. It is based on the analysis of the sub-threshold spontaneous emission spectrum, as illustrated in Fig. 2.7. The gain and wavelength evolution of this amplified spontaneous emission spectrum with the bias current directly gives the α -factor since:

$$\frac{d\lambda}{\lambda} = \frac{dn}{n} \quad (2.28)$$

For this method, one must however be careful to consider solely the wavelength shift due to the carrier density evolution and not that due to the heating of the structure when increasing the bias current even below threshold.

However, studies have shown that, above threshold, some additional effects such as gain compression significantly impact the α -factor. For instance, LEF values between 0.1 and 0.7 have been reported in InAs quantum-dot lasers far below threshold, before the appearance of gain saturation [29]. Therefore, several other methods have been developed to measure the above-threshold, room-temperature linewidth broadening factor [30]. For instance, it can be retrieved from the FM-AM ratio of the laser under modulation, as illustrated by Fig. 2.8a. At high modulation frequency $f_m \gg f_c$, where f_c is the corner frequency, by defining β and m the modulation indices in frequency and amplitude, respectively, the $2\beta/m$ coefficient reaches a plateau where:

$$\frac{2\beta}{m} = \alpha \sqrt{1 + \left(\frac{f_c}{f_m}\right)^2} \rightarrow \alpha \quad (2.29)$$

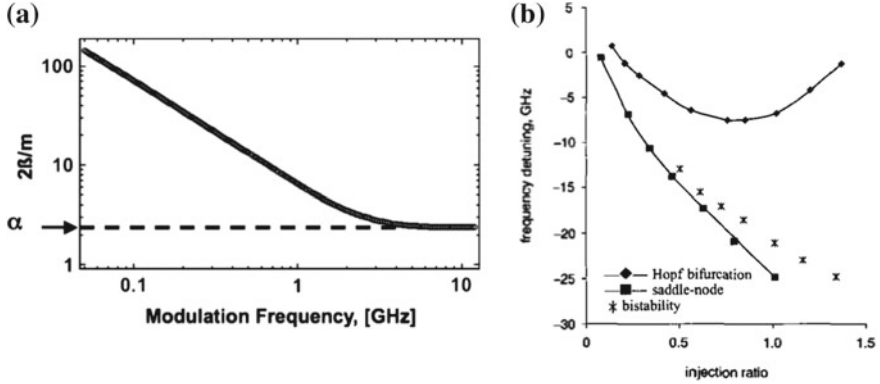


Fig. 2.8 **a** Measurement of the α -factor using FM-AM ratio (courtesy of [30]). **b** Minimum of the Hopf bifurcation of a laser under optical injection, giving a LEF of 3.2 (courtesy of [31])

As shown in Fig. 2.8b, the LEF can also be retrieved from the minimum point of the Hopf bifurcation ω_{min} of the semiconductor laser under optical injection, i.e. the limit curve between stable and unstable locking, since [31]:

$$\omega_{min} \approx -\sqrt{\frac{(\alpha^2 - 1)^3}{32\alpha^2}} \quad (2.30)$$

This method gives an effective α -factor, which value depends on the operating conditions of the device. However, in the limit case where the laser is operated just above threshold, this effective LEF should be equal to the material LEF obtained with other techniques.

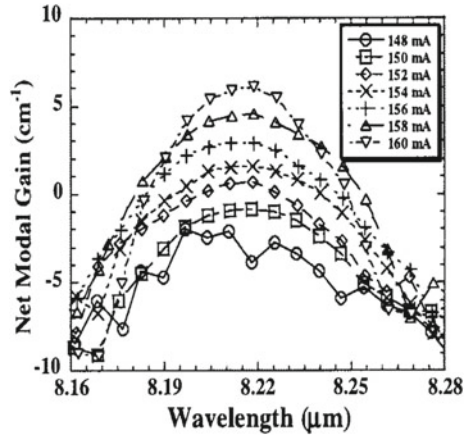
Recently, a new technique has been proposed by Wang et al. [32], also based on optical injection. By injecting far from the maximum gain mode of a Fabry-Perot laser, and studying the evolution of the residual side-mode under stable injection locking when modifying the master laser frequency, the α -factor can be retrieved from the expression:

$$\alpha = -\frac{2\pi}{L\delta\lambda} \frac{d\lambda/d\lambda_m}{dG_{net}/d\lambda_m} \quad (2.31)$$

where λ_m is the master laser wavelength. Although the measurements are performed above threshold, this method is insensitive to thermal effects, bias current or choice of injection-locked mode and gives the material sub-threshold α -factor.

Typically, the LEF values reported for quantum well lasers range from 1 to 3, whereas for more complex structures, such as quantum dot lasers, the α -factor is higher, between 3 and 10 [33]. A record value as high as $\alpha = 57$ in InAs quantum dot lasers emitting both on ground state and excited state has even been reported [34].

Fig. 2.9 Experimental gain curve of a QCL, showing good symmetry (courtesy of [35])



2.3.3 α -Factor of QCLs

An estimation of the α -factor can be obtained based on the gain asymmetry. As shown previously, the gain of a QCL has the shape of a Lorentzian and is almost symmetrical (see Fig. 2.9), the linewidth broadening factor of a QCL was therefore expected to be almost zero.

Based on the Lorentzian lineshape of the QCLs, another theoretical expression can be deduced from the linewidth equation [15]:

$$\alpha_{QCL}(\nu) = - \left(\frac{\nu - \nu_{32}}{\gamma_{32}} \right) \quad (2.32)$$

with ν_{32} the center frequency of the gain spectrum and γ_{32} its half-width at half-maximum. This expression leads to a theoretical zero linewidth broadening factor at the center frequency, and to very small values around the peak for DFB QCLs.

Typically for mid-infrared QCLs, the measured sub-threshold α -factor using this Hakki-Paoli technique varies between -0.6 and 0.3 [35–37]. This value is low, but definitely non-zero. It is also important to point out, that most of these measurements were performed at cryogenic temperature. When increasing the temperature up to 300 K, thermal agitation of phonons will lead to broader linewidth, and hence to higher linewidth broadening factor values.

Furthermore, the spatial hole burning is very large in QCLs compared to laser diodes [38] and the above-threshold α -factor is expected to be significantly different from that measured below threshold. There are very few reports of above-threshold linewidth broadening factor measurements at room temperature for a mid-infrared QCL. Using the fit of the L-I curves while controlling the internal laser temperature, Hangauer et al. [39] reported values between 0.167 and 0.483 close to threshold. Moreover, von Staden et al. [40] deduced the α -factor from the self-mixing inter-

ferometers and obtained values between 0.26 and 2.4, strongly increasing with the bias current. One measurement of the FM-AM ratio using optical heterodyning led to α -factor values of 0.02 ± 0.2 at 243 K [41]. This measurement has the advantage at high frequency to be independent of the thermal effects, but it might lead to some issues when considering structures with complex carrier dynamics, such as quantum dot lasers or QCLs. It would be interesting to apply techniques such as optical injection far from the maximum gain mode to measure the LEF of a QCL, to obtain temperature independent values.

2.4 Detailed Study of a QCL Design

In this thesis, we will focus mainly on a specific QCL structure that produced performant lasers, both Fabry-Perot and DFB, emitting around $5.6 \mu\text{m}$.

2.4.1 Fabrication of QCL Devices

The active area follows a custom design inspired by [42] and consists of 30 periods of AlInAs/GaInAs grown by molecular beam epitaxy on a low-doped (10^{17} cm^{-3}) InP cladding. The upper InP cladding is then grown by metal organic chemical vapor epitaxy. In the case of the DFB QCL, the upper cladding was designed following [43] to enable single-mode emission. A top metal grating was added, with a coupling efficiency of $\kappa \approx 4 \text{ cm}^{-1}$, leading to a κL is close to unity. Contrary to buried gratings or conventional top gratings with a highly doped dielectric layer between the cladding and the grating, which are based on gain-guiding, this technology is based on index-guiding. The modulation of the refractive index originates from the coupling between the guided modes in the active region and the surface mode, also called plasmon-polariton, which is confined at the interface between metal and upper cladding, two materials with permittivities of opposite signs [14].

The wafer is then processed using double-trench technology, in order to reduce the lateral current spreading in the device, and therefore to reduce the self-heating of the laser [15, 44].

To improve the performances, a high-reflectivity (HR) coating ($R > 95\%$) on the back facet reduces mirror losses, while the front facet is leaved as cleaved ($R = 0.3$). Finally, for efficient heat extraction, the QCL is most of the time epispide-down mounted with gold-tin soldering on AlN submount. Figure 2.10 shows a schematic and a scanning electron microscopy (SEM) picture of the DFB device under study.

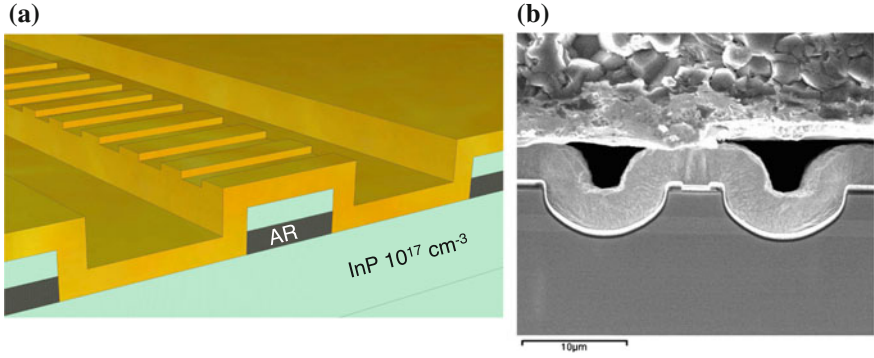


Fig. 2.10 **a** Schematic and **b** SEM picture of the DBF QCL under study. The active region, labeled ‘AR’ in (a), appears in (b) in lighter gray

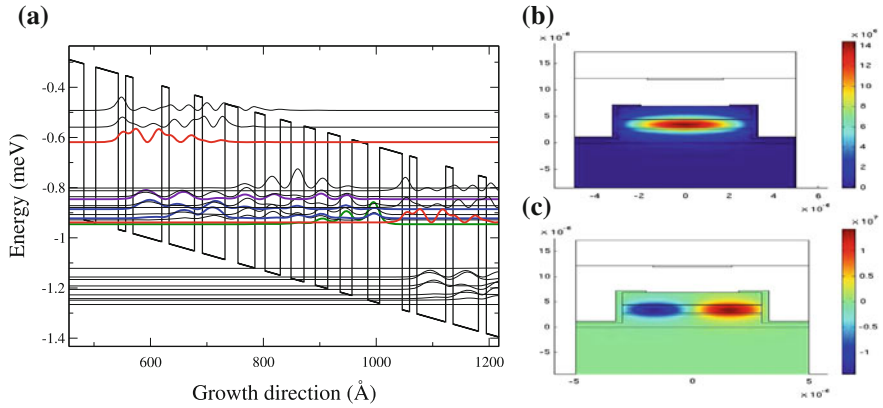


Fig. 2.11 **a** Wave functions of the QCL structure under study, simulated with METIS. In *red*, levels |3> of two consecutive periods, in *violet* level |2>, in *blue* level |1> split into two phonon states, in *green* injector state. **b** Fundamental mode TM0 simulation using COMSOL. **c** TM1 simulation

2.4.2 QCL Internal Parameters

Most internal parameters of the laser are properties of the active area design and can be retrieved using a homemade heterostructure simulation software named METIS. It is based on semi-classical Boltzmann-like equations with thermalized subbands and takes into account coherent tunneling through the barrier, optical and acoustic longitudinal phonons, absorption of photons, roughness scattering and spontaneous and stimulated emission. The potential, energy states, wave functions and electronic scattering times can be calculated, with very good agreement between simulation and experiment [45]. The active area design and wave-functions of the studied QCL are represented in Fig. 2.11 a.

Table 2.1 Laser parameters

| Parameter | Value (ps) | Parameter | Value |
|----------------------------------|------------|-----------------------------------|----------------------------------|
| Carrier lifetime 3-2 τ_{32} | 2.27 | Group index n_g | 3.2 |
| Carrier lifetime 3-1 τ_{31} | 2.30 | Confinement factor Γ_{opt} | 68% |
| Carrier lifetime 2-1 τ_{21} | 0.37 | Net modal gain G_0 | $1.2 \times 10^4 \text{ s}^{-1}$ |
| Carrier escape time τ_{out} | 0.54 | Photon lifetime τ_p | 4.74 ps |

Furthermore, the repartition of the modes inside the QCL can be simulated using COMSOL, as shown in Fig. 2.11b and c, presenting the simulations of the fundamental mode TM0 and first order mode TM1, respectively. The group refractive index and the confinement factor can be retrieved.

All the simulated parameters of the specific structure under study are summarized in Table 2.1. The missing values are the conversion efficiency η , ratio between the optical and electrical powers, which depends on each device and will be retrieved from the L-I characteristic curves, as well as the α -factor, which measurement will be developed later on.

2.4.3 Laser Static Properties

For the following experiments, it is necessary to know precisely the characteristics and performances of the QCLs under study in free-running operation, i.e. without any external perturbations. These lasers are based on the active region previously described.

The DFB QCLs are 2 mm long and 9 μm wide, there are epi-side down mounted with a high-reflectivity coating on the back facet. The lasers can be operated both in continuous-wave and pulsed mode. The L-I-V characteristic curves of such a QCL in continuous-wave operation at 10°, 20°, 30° and 40°C are represented in Fig. 2.12a. For instance, at 20°C, the laser threshold is at 421 mA (current density of $J_{th} = 2.34 \text{ kA/cm}^2$), and 9.22 V and the maximum emitted power is 140.4 mW, but these characteristics may slightly vary from one laser to the other and depending on the current source and detection optics used in the experimental setup. The dip that appears sometimes in the L-I curves, for instance at 581 mA at 10°C, is a measurement artifact due to the strong water absorption on the path between laser and detector at this wavelength.

As shown in Fig. 2.12b, the DFB QCLs are perfectly single-mode all along the L-I curve, and the wavelength red-shifts from 1769.5 cm^{-1} (5.651 μm) to 1764.4 cm^{-1} (5.668 μm) when increasing the bias current. Finally, the far-field of the DFB QCL is drawn in Fig. 2.12c, presenting a relatively round beam. The full width at half maximum of the far-field is 47° horizontally and 59° vertically.

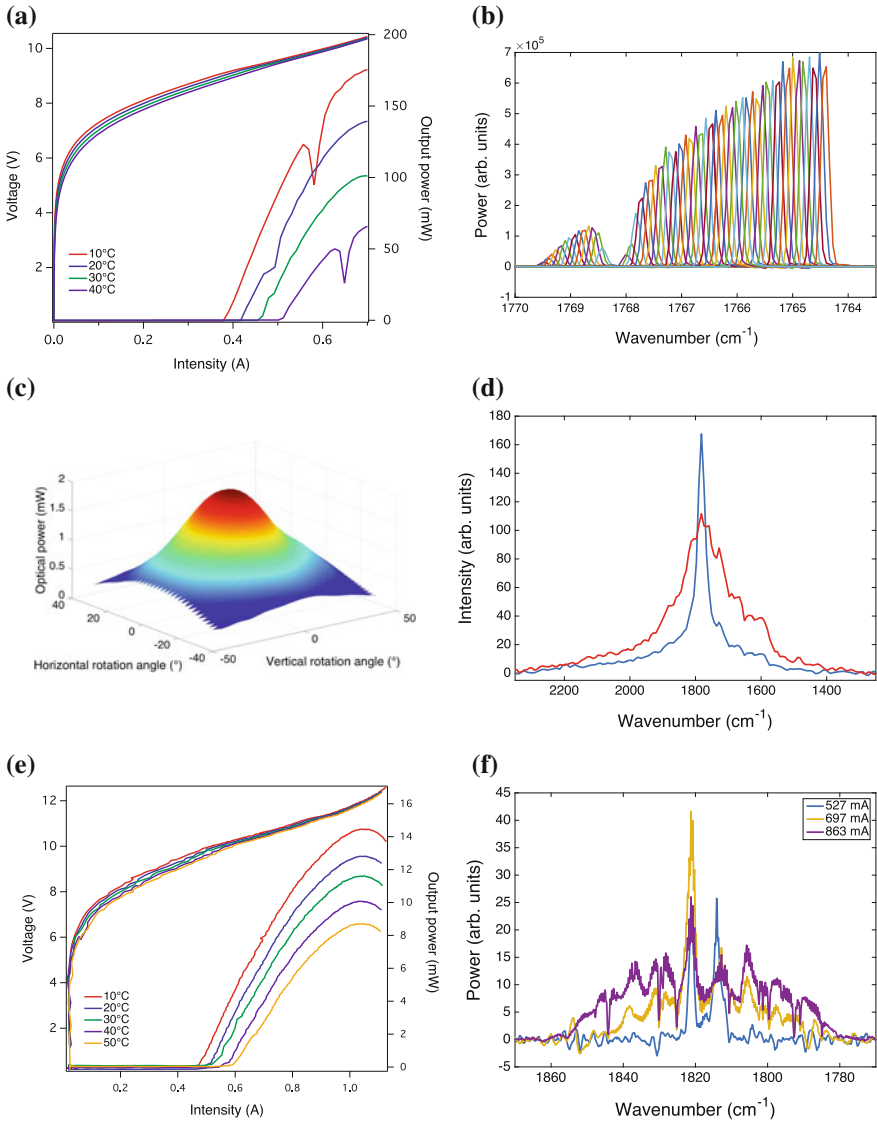


Fig. 2.12 **a** L-I-V characteristic curves of a 2 mm × 9 μm epi-down DFB QCL operated in continuous-wave at different temperatures. **b** Corresponding optical spectra at 20 °C for several bias current, showing the wavelength *red-shift* with active area heating. **c** Far-field of the DFB QCL. **d** Electroluminescence spectra of the DFB QCL far from threshold (*in red*) and just below threshold (*in blue*). **e** L-I-V characteristic curves of a 3 mm × 6 μm epi-up FP QCL operated in pulsed mode (100 kHz, 300 ns) at different temperatures. **f** Optical spectra of the same laser at 300 ns, 50 kHz and 15 °C for several bias current, showing the broadening of the FP spectrum

Figure 2.12d presents the electroluminescence spectra of the DFB QCL, measured in pulsed mode, with a pulse length of 300 ns and a repetition rate of 100 kHz, using a lock-in amplifier and sensitive mercury-cadmium-telluride (MCT) photodetector at cryogenic temperature. The red curve corresponds to a measurement far below threshold, where the electroluminescence spectrum follows the gain shape. It is centered around 1782 cm^{-1} ($5.61 \text{ }\mu\text{m}$) and its full width at half maximum (FWHM) is 138 cm^{-1} (FWHM = $44 \text{ }\mu\text{m}$ expressed in wavelength). Furthermore, it is worth noticing that the spectrum is not perfectly symmetrical, which suggests a non-symmetrical gain, and hence a non-zero α -factor. The blue curve was measured just below threshold. In this case, the electroluminescence spectrum is much narrower, with a FWHM of 15 cm^{-1} (FWHM = $5 \text{ }\mu\text{m}$ in terms of wavelength), showing clear gain saturation.

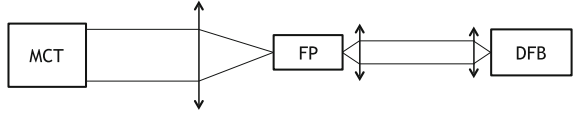
Several Fabry-Perot QCLs are used depending on the performances needed for the experiments. One of them is epi-side up mounted and cleaved on both facets, with a 3 mm-long and $6 \text{ }\mu\text{m}$ -wide active region. The others are epi-side down mounted with a high-reflectivity coating on the back facet, their dimensions are $3 \text{ mm} \times 6 \text{ }\mu\text{m}$, $4 \text{ mm} \times 6 \text{ }\mu\text{m}$ and $4 \text{ mm} \times 12 \text{ }\mu\text{m}$, respectively. The thermal management of the epi-up QCL is less efficient, and therefore the laser can only be operated in pulsed mode. Figure 2.12e shows the L-I-V curves of this laser at several temperatures. At 20°C , with pulses of 300 ns and a repetition rate of 100 kHz, the threshold is around 499 mA ($J_{th} = 2.77 \text{ kA/cm}^2$) and 9.87 V, and the maximum emitted power is around 13 mW. From the threshold measurements at different temperatures between 10 and 50°C , the T_0 of the laser can be extracted, with:

$$I(T) = I_0 e^{T/T_0} \quad (2.33)$$

For this structure, the extracted value is $T_0 = 184 \text{ K}$ between 10 and 50°C , which is of the order of magnitude of the usual values in QCL structures [15]. The epi-down lasers have better thermal management and can therefore achieve higher optical powers. The $3 \text{ mm} \times 6 \text{ }\mu\text{m}$ QCL threshold is located at 591 mA ($J_{th} = 3.28 \text{ kA/cm}^2$) and 9.50 V and the laser emits up to 72 mW in continuous-wave mode at 20°C . The $4 \text{ mm} \times 6 \text{ }\mu\text{m}$ QCL starts to lase at 843 mA ($J_{th} = 3.51 \text{ kA/cm}^2$) and 9.85 V and the laser emits up to 50 mW. Finally, the $4 \text{ mm} \times 12 \text{ }\mu\text{m}$ QCL has its threshold at 1.20 A ($J_{th} = 2.5 \text{ kA/cm}^2$) and 8.87 V and can emit up to 255 mW.

The optical spectra of the epi-up FP QCL at 15°C , with pulses of 300 ns and a repetition rate of 50 kHz, are represented in Fig. 2.12f for several bias currents, clearly showing the broadening of the gain and hence of the FP spectrum when increasing the pump current. In this case, the center frequency is around 1820 cm^{-1} ($5.45 \text{ }\mu\text{m}$), but it can vary depending on the laser geometry.

Fig. 2.13 Experimental setup for the below threshold gain measurements



2.4.4 QCL Gain Measurements

The gain of the QCL structure can be measured using the method proposed by Benveniste et al. [46]. It consists in injecting the light emitted by a DFB QCL into a Fabry-Perot QCL operated below threshold, as depicted in Fig. 2.13. In our case, the DFB QCL is 2 mm long and 9 μm wide and runs in continuous-wave, whereas the Fabry-Perot laser is 3 mm long and 6 μm wide, cleaved on both facets and operated in pulsed mode.

The temporal chirp during the pulse will lead to the appearance of fringes in the optical power time traces, which can be fitted with Airy function when expressed as a function of the chirp or refractive index variations, as shown in Fig. 2.14a. The gain of the Fabry-Perot QCL can then be retrieved from:

$$G - \alpha_M - \alpha_{ISB} - \alpha_W = \frac{1}{L} \ln \left(\frac{k-1}{k+1} \right) \quad (2.34)$$

with L the laser length and $k = \sqrt{I_{\max}/I_{\min}}$, where I_{\max} and I_{\min} are two consecutive maximum and minimum of the DFB optical intensity transmitted through the Fabry-Perot laser. The mirror losses are $\alpha_M = 4 \text{ cm}^{-1}$. The waveguide losses α_W can be estimated by studying the transverse electrical (TE) transmission of the DFB through the Fabry-Perot. However, it was not possible in our setup to rotate the Fabry-Perot QCL, and the value was taken at $\alpha_W \approx 10 \text{ cm}^{-1}$, as measured in a previous work for a similar DFB QCL. However, this value varies significantly from one device to the other, especially with the laser length, and must therefore be considered carefully. Finally, the intersubband losses α_{ISB} could be extracted from a measurement far below threshold, where the gain is negligible. However, no signal was detected at such a low bias current, and these losses could not be extracted for this QCL. The evolution of $G - \alpha_{ISB} - \alpha_W$ with the Fabry-Perot current density is presented in Fig. 2.14b, when the DFB QCL is operated at 589 mA and 9.8 V.

The last point of Fig. 2.14b was measured just below threshold. However, at threshold we expect $G - \alpha_M - \alpha_{ISB} - \alpha_W = 0$, which is not the case in our measurement. This could be explained by the existence of a shift between the maximum gain peak and the DFB wavelength, leading to gain measurement that does not correspond to the maximum gain equal to the total losses at threshold [46]. Indeed, from the electroluminescence spectrum (Fig. 2.12d), we deduce that the laser hits the gain at about 92% of its maximum and we expect a maximum gain of $G_{\max} = 0.92 \times (\alpha_m + \alpha_W + \alpha_{ISB})$, although it can not be verified here.

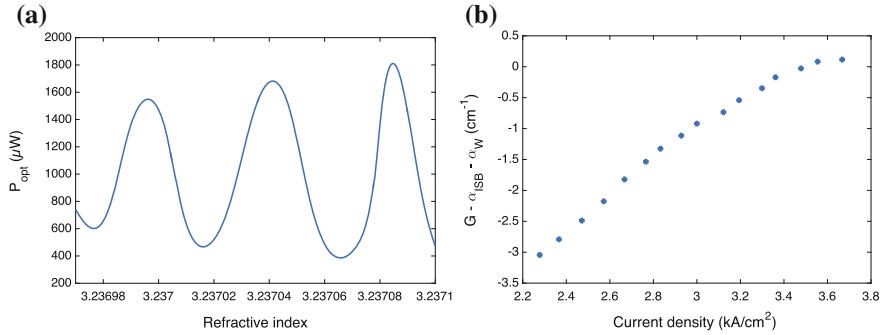
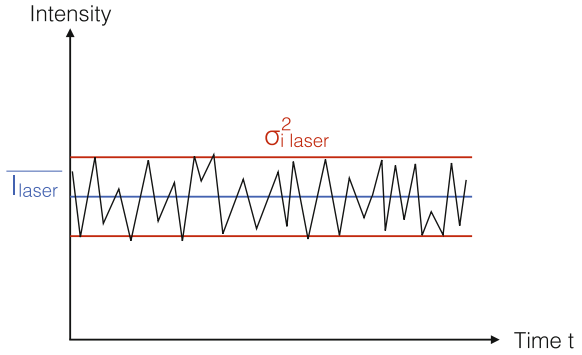


Fig. 2.14 **a** DFB transmitted intensity as a function of the FP refractive index, for a current density in the Fabry-Perot laser of 3.35 kA/cm^2 . **b** Fabry-Perot QCL modal gain evolution as a function of the bias current below threshold, at constant DFB laser operating conditions 589 mA and 9.8 V

Fig. 2.15 Definition of the RIN



2.4.5 Intensity Noise Measurements

For a given intensity emitted by the laser $I_{laser}(t) = \overline{I_{laser}} + i(t)$, the linear relative intensity noise (RIN) is defined as:

$$RIN = \frac{\overline{i^2}}{\overline{I_{laser}}^2} = \frac{\sigma_{i_{laser}}^2}{\overline{I_{laser}}^2} \quad (2.35)$$

where $\overline{I_{laser}}$ is the average flux intensity and $i(t)$ the temporal fluctuations of the emitted signal, and $\sigma_{i_{laser}}^2$ the variance of the laser noise, as defined in Fig. 2.15.

This laser noise originates mainly from the beating between stimulated and spontaneous emissions [47]. The existence of spontaneous emission indeed leads to photons with random polarization, direction and phase, that will compete with the coherent light from stimulated emission and generate noise.

A good knowledge of the RIN is important for spectroscopic applications. The signal to noise ratio (SNR), quantifying the sensitivity of the detector, indeed depends

on the detected signal I_{signal} , directly proportional to the flux intensity emitted by the laser I_{laser} and on the noise standard deviation, $\sigma_{i total}$, which takes into account all noises including laser noise, background noise and detection noise (detector thermal and photon noise and preamplifier noise):

$$SNR = \frac{I_{signal}}{\sigma_{i total}} \quad (2.36)$$

Therefore, the SNR depends on the RIN. In the case of optical spectroscopy, the detected signal intensity is directly proportional to the light intensity emitted by the laser and to the absorbance α_{abs} , with $I_{signal} = \alpha_{abs} I_{laser}$. Therefore, the SNR can be expressed as:

$$SNR = \sqrt{\frac{t}{RIN}} \alpha_{abs} \quad (2.37)$$

with t the integration time.

In this paragraph, the RIN of a DFB QCL is measured both in continuous-wave and pulsed operation, in order to conclude whether the studied QCL structure can be used for spectroscopic applications.

The RIN can be retrieved from the signal detected on a photodiode, here a MCT detector operating at cryogenic temperature. After a preamplifier with a gain coefficient $V = 100$, the electrical signal is analyzed simultaneously on a real-time scope and on an electrical spectrum analyzer (ESA). The average DC signal U_{DC} is measured on the scope and the AC signal corresponding to the mean value of the electrical spectrum at a given frequency ν , $Sp(\nu)$, is measured for a given resolution bandwidth B of the ESA, here 200 Hz. The center frequency ν can be taken in the frequency range of the detector, by carefully avoiding the range where the signal is dominated by the $1/f$ noise of the detector, in our case between 10 kHz and 1 MHz. The RIN at a given frequency can be expressed as:

$$RIN(\nu) = \frac{Sp(\nu)R_{ESA}}{U_{DC}^2 BV} \quad (2.38)$$

where R_{ESA} is the input resistance of the ESA. The usual unity of a RIN is dB/Hz. The uncertainty of the RIN obtained with this method is 2 dB/Hz, calculated over 10 measurements.

The RIN of the DFB QCL operated in continuous-wave was measured at TU Darmstadt with two different sources : a commercial one, ILX, and a homemade low-noise battery. The RIN at 400 kHz is plotted in Fig. 2.16 as a function of the normalized pump parameter $a = I/I_{th} - 1$, showing an exponential decrease of the RIN when increasing the pump current, with values ranging from -110 and -155 dB/Hz.

The RIN of the laser using the ARMEXEL source at a repetition rate of 100 kHz is measured under several operating conditions. In pulsed mode, the RIN does not decrease exponentially with the bias current as in continuous-wave operation, but oscillates around -110 dB/Hz after a short decrease for low bias currents.

Fig. 2.16 Continuous-wave RIN values for two different sources at 400 kHz

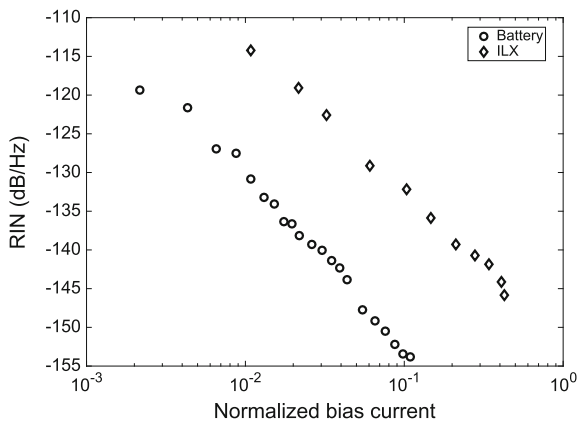


Figure 2.17a presents the RIN at different center frequencies within the detector range, showing little dependence of the RIN with the measurement frequency. However, the study of the RIN evolution with the pulse width at a fixed center frequency of 20 kHz shows that a longer pulse duration results in a lower RIN (Fig. 2.17b).

The RIN measurements are repeated with the PICOLAS source at a repetition rate of 100 kHz. The RIN evolution with the bias current has the same tendency as with the ARMEXEL source, and oscillates around the same value of -110 dB/Hz after a short decrease for low bias currents. The study of the RIN at different center frequencies (Fig. 2.17c) shows that this source is optimized at higher frequency, with a RIN decreasing as the measurement frequency increases. However, the RIN remains almost constant with the pulse duration at a center frequency of 20 kHz (Fig. 2.17d).

The laser noise, characterized by the RIN, is therefore stronger in pulsed operation than in continuous wave. The intensity fluctuations in pulsed mode originate from the temporal variations of the pulse duration and period, as well as from amplitude fluctuations between two consecutive pulses.

The measured RIN values are higher than the typical ones for single-mode inter-band laser diodes (around -160 dB/Hz, see [47]), but are consistent with other measurements realized on QCLs [48]. Typical RIN values acceptable for spectroscopic applications are below -150 dB/Hz. The QCL under study can therefore be used for spectroscopy easily in continuous-wave, but also in pulsed mode by averaging over a longer acquisition time t , since the key parameter remains the SNR, which is proportional to \sqrt{t} . This can be a drawback for some applications, but several techniques can be implemented to improve the SNR, such as matched filter, synchronous detection or use of a reference path.

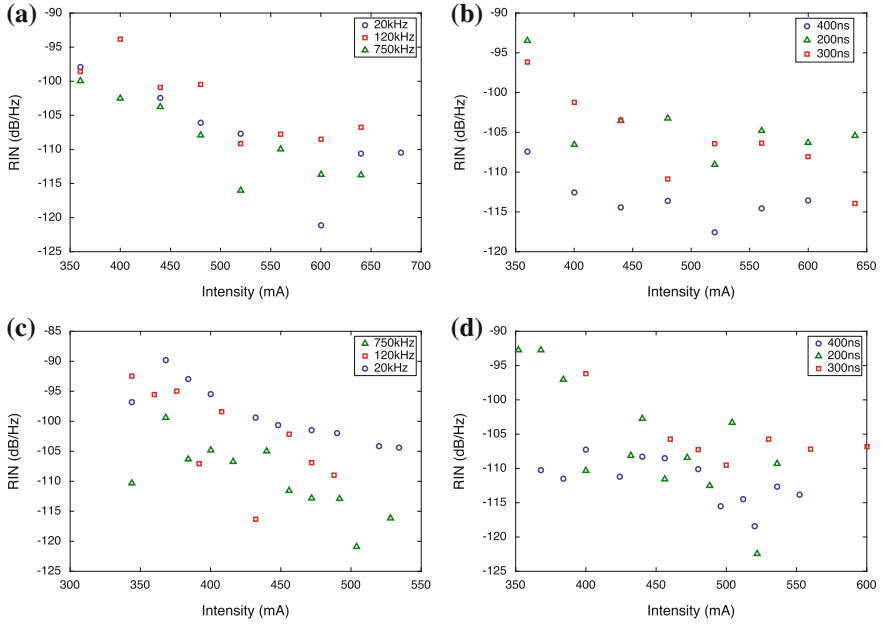


Fig. 2.17 **a** ARMEXEL RIN evolution with current for 300 ns pulses at 100 kHz at several measurement frequencies. **b** ARMEXEL RIN evolution with current at a repetition rate of 100 kHz measured at 20 kHz for several pulse widths. **c** PICOLAS RIN evolution with current for 300 ns pulses at 100 kHz at several measurement frequencies. **d** PICOLAS RIN evolution with current at a repetition rate of 100 kHz measured at 20 kHz for several pulse widths

2.5 Conclusions

In this chapter, the QCL technology has been studied. Thanks to their intersubband transitions, the QCLs can operate from 3 μm up to 250 μm , depending on the active region design. They are compact sources with high output power, and have therefore become favored laser sources for mid-infrared applications.

The specific QCL design that will be used in the following chapters has been characterized in details. Both Fabry-Perot and DFB QCLs emitting around 5.6 μm are available, with output power as high as 255 mW in continuous wave operation at 20°C.

References

1. R.F. Kazarinov, R.A. Suris, Possibility of the amplification of electromagnetic waves in a semiconductor with a superlattice. *Sov. Phys. Semicond.* **5**(4), 707–709 (1971)
2. J. Faist, F. Capasso, D.L. Sivco, C. Sirtori, A.L. Hutchinson, A.Y. Cho, Quantum Cascade Laser. *Science* **264**(5158), 553–556 (1994)
3. M. Beck, D. Hofstetter, T. Aellen, J. Faist, U. Oesterle, M. Ilegems, E. Gini, H. Melchior, Continuous wave operation of a mid-infrared semiconductor laser at room temperature. *Science* **295**, 301–305 (2002)
4. M. Razeghi, S. Slivken, Y. Bai, B. Gokden, S.R. Darvish, High power quantum cascade lasers. *New J. Phys.* **11**(12), 125017 (2009)
5. Y. Bai, N. Bandyopadhyay, S. Tsao, S. Slivken, M. Razeghi, Room temperature quantum cascade lasers with 27% wall plug efficiency. *Appl. Phys. Lett.* **98**, 181102 (2011)
6. M.S. Vitiello, G. Scalari, B. Williams, P.D. Natale, Quantum cascade lasers: 20 years of challenges. *Opt. Express* **23**(4), 5167–5182 (2015)
7. R. Koehler, A. Tredicucci, F. Beltram, H.E. Beere, E. Linfield, A. Davies, D. Ritchie, R. Iotti, F. Rossi, Terahertz semiconductor-heterostructure laser, vol. 417, pp. 156–159 (2002)
8. A. Wade, G. Fedorov, D. Smirnov, S. Kumar, B.S. Williams, Q. Hu, J.L. Reno, Magnetic-field-assisted terahertz quantum cascade laser operating up to 225 K. *Nat. Photon.* **3**, 41–45 (2009)
9. M. Belkin, F. Capasso, F. Xie, A. Belyanin, M. Fischer, A. Wittmann, J. Faist, Room temperature terahertz quantum cascade laser source based on intracavity difference frequency generation. *Appl. Phys. Lett.* **92**, 201101 (2008)
10. J. Devenson, O. Cathabard, R. Tessier, A.N. Baranov, InAs/AlSb quantum cascade laser emitting at 2.75–2.97 μm . *Appl. Phys. Lett.* **91**, 251102 (2007)
11. C. Gmachl, F. Capasso, D.L. Sivco, A.Y. Cho, Recent progress in quantum cascade lasers and applications. *Rep. Prog. Phys.* **64**(11), 1533 (2001)
12. G. Bastard, *Wave Mechanics Applied to Semiconductor Heterostructures* (Les éditions de physique, Paris, 1990)
13. R. Maulini, Broadly tunable mid-infrared quantum cascade laser for spectroscopic applications, Ph.D. dissertation, Université de Neuchâtel, 2006
14. G. Maisons, Réalisation de sources lasers monomodes innovantes émettant dans le moyen infrarouge. Application à la spectroscopie. Ph.D. dissertation, Université de Grenoble, 2010
15. J. Faist, *Quantum Cascade Lasers* (Oxford University Press, 2013)
16. Y. Petitjean, F. Destic, J.C. Mollier, C. Sirtori, Dynamic modeling of terahertz quantum cascade lasers. *IEEE J. Sel. Top. Quantum Electron.* **17**(1), 22–29 (2011)
17. G. Agrawal, *Long-Wavelength Semiconductor Lasers*, Ser. Van Nostrand Reinhold Electrical/Computer Science and Engineering Series (Springer, Netherlands, 1986)
18. F. Rana, R.J. Ram, Current noise and photon noise in quantum cascade lasers, *Phys. Rev. B* **65**, 125 313–125 342 (2002)
19. R. Paiella, R. Martini, F. Capasso, C. Gmachl, H.Y. Hwang, D.L. Sivco, J.N. Baillargeon, A.Y. Cho, E.A. Whittaker, H.C. Liu, High-frequency modulation without the relaxation oscillation resonance in quantum cascade lasers. *Appl. Phys. Lett.* **79**(16), 2526–2528 (2001)
20. A.L. Schawlow, C.H. Townes, Infrared and optical masers. *Phys. Rev.* **112**(6), 1940–1949 (1958)
21. M. Lax, Quantum noise. X. Density-matrix treatment of field of population difference fluctuations. *Phys. Rev.* **157**(2), 213–231 (1967)
22. H. Haug, H. Haken, Theory of noise in semiconductor laser emission. *Z. Phys.* **204**, 262–275 (1967)
23. C.H. Henry, Theory of the linewidth of semiconductor lasers. *IEEE J. Quantum Electron.* **18**, 259–264 (1982)
24. J.R. Marcante, G.P. Agrawal, Nonlinear mechanisms of filamentation in broad-area semiconductor lasers. *IEEE J. Quantum Electron.* **32**(4), 590–596 (1996)

25. M. Osinski, J. Buus, Linewidth broadening factor in semiconductor lasers-an overview. *IEEE J. Quantum Electron.* **23**(1), 9–29 (1987)
26. B.W. Hakki, T.L. Paoli, Gain spectra in GaAs double heterostructure injection lasers. *J. Appl. Phys.* **46**(3), 1299–1306 (1975)
27. I.D. Henning, J. Collins, Measurement of the semiconductor linewidth broadening factor. *Electron. Lett.* **19**(22), 927–929 (1983)
28. H. Huang, K. Schires, P.J. Poole, F. Grillot, Non-degenerate four-wave mixing in an optically injection-locked InAs/InP quantum dot Fabry-Perot laser. *Appl. Phys. Lett.* **106**, 143501 (2015)
29. T.C. Newell, D.J. Bossert, A. Stintz, B. Fuchs, K.J. Malloy, L.F. Lester, Gain and linewidth enhancement factor in InAs quantum-dot laser diodes. *IEEE Photon. Technol. Lett.* **11**(12), 1527–1529 (1999)
30. J.G. Provost, F. Grillot, Measuring the chirp and the linewidth enhancement factor of optoelectronic devices with a Mach-Zehnder interferometer. *IEEE Photon. J.* **3**(3), 476–488 (2011)
31. K.E. Chlouverakis, K.M. Al-Aswad, I.D. Henning, M.J. Adams, Determining laser linewidth parameter from hopf bifurcation minimum in lasers subject to optical injection. *Electron. Lett.* **39**(16), 1185–1187 (2003)
32. C. Wang, K. Schires, M. Osinski, P.J. Poole, F. Grillot, Thermally insensitive determination of the linewidth broadening factor in nanostructured semiconductor lasers using optical injection locking. *Sci. Rep.* **6**, 27825 (2016)
33. C. Wang, Modulation dynamics of InP-based nanostructure laser and quantum cascade laser, Ph.D. dissertation, INSA Rennes, 2015
34. B. Dagens, A. Markus, J.X. Chen, J.-G. Provost, D. Make, O.L. Guezizigou, J. Landreau, A. Fiore, B. Thedrez, Giant linewidth enhancement factor and purely frequency modulated emission from quantum dot laser. *Electron. Lett.* **41**(6), 323–324 (2005)
35. M. Lerttamrab, S.L. Chuang, C. Gmachl, D.L. Sivco, F. Capasso, A.Y. Cho, Linewidth enhancement factor of a type-I quantum cascade laser. *J. Appl. Phys.* **94**(8), 5426–5428 (2003)
36. J. Kim, M. Lerttamrab, S.L. Chuang, C. Gmachl, D.L. Sivco, F. Capasso, A.Y. Cho, Theoretical and experimental study of optical gain and linewidth enhancement factor of type I quantum cascade lasers. *IEEE J. Quantum Electron.* **40**(12), 1663–1674 (2004)
37. T. Liu, K.E. Lee, Q.J. Wang, Importance of the microscopic effects on the linewidth enhancement factor of quantum cascade lasers. *Opt. Express* **21**(23), 27 804–27 815 (2013)
38. A. Gordon, C.Y. Wang, L. Diehl, F.X. Kärtner, A. Belyanin, D. Bour, S. Corzine, G. Höfler, H.C. Liu, H. Schneider, T. Maier, M. Troccoli, J. Faist, F. Capasso, Multimode regimes in quantum cascade lasers: From coherent instabilities to spatial hole burning. *Phys. Rev. A* **77**, 053804 (2008)
39. A. Hangauer, G. Wysocki, Gain compression and linewidth enhancement factor in mid-IR quantum cascade lasers. *IEEE J. Sel. Top. Quantum Electron.* **21**(6), 1200411 (2015)
40. J. von Staden, T. Gensty, M. Peil, W. Elsässer, G. Giuliani, C. Mann, Measurements of the α factor of a distributed-feedback quantum cascade laser by an optical feedback self-mixing technique. *Opt. Lett.* **31**(17), 2574–2576 (2006)
41. T. Aellen, R. Maulini, R. Terazzi, N. Hoyler, M. Giovannini, J. Faist, S. Blaser, L. Hvoz-dara, Direct measurement of the linewidth enhancement factor by optical heterodyning of an amplitude-modulated quantum cascade laser. *Appl. Phys. Lett.* **89**, 091121 (2006)
42. A. Evans, J.S. Yu, J. David, L. Doris, K. Mi, S. Slivken, M. Razeghi, High-temperature, high-power, continuous-wave operation of buried heterostructure quantum-cascade lasers. *Appl. Phys. Lett.* **84**(3), 314–316 (2004)
43. M. Carras, G. Maisons, B. Simozrag, M. Garcia, O. Parillaud, J. Massies, X. Marcadet, Room-temperature continuous-wave metal grating distributed feedback quantum cascade lasers. *Appl. Phys. Lett.* **96**(16), 161105 (2010)
44. A. Szerling, P. Karbownik, K. Kosiel, J. Kubacka-Traczyk, E. Pruszyńska-Karbownik, M. Pluska, M. Bugajski, Mid-infrared GaAs/AlGaAs quantum cascade lasers technology. *Acta Phys. Pol. A* **116**, S45–S48 (2009)
45. V. Trinité, E. Ouerghemmi, V. Guériaux, M. Carras, A. Nedelcu, E. Costard, J. Nagle, Modelling of electronic transport in quantum well infrared photodetectors. *Infrared Phys. Techn.* **54**(3), 204–208 (2011)

- 46. E. Benveniste, S. Laurent, A. Vasanelli, C. Manquest, C. Sirtori, F. Teulon, M. Carras, X. Marcadet, Measurement of gain and losses of a mid-infrared quantum cascade laser by wavelength chirping spectroscopy. *Appl. Phys. Lett.* **94**, 081110 (2009)
- 47. K. Petermann, *Laser Diode Modulation and Noise* (Springer, 1988)
- 48. C. Juretzka, H. Simos, A. Bogris, D. Syvridis, W. Elsaber, M. Carras, Intensity noise properties of mid-infrared injection locked quantum cascade lasers: II. Experiments. *IEEE J. Quantum Electron.* **51**(1), 1–8 (2015)

Nonlinear Photonics in Mid-infrared Quantum Cascade
Lasers

Jumpertz, L.

2017, XXIII, 134 p. 100 illus., 6 illus. in color., Hardcover

ISBN: 978-3-319-65878-0